Fe single atoms coupled Fe_3C multi-functional catalysts on P, F, N-doped carbon nanotubes for stable Zn-air batteries with ultra-high power densities

Manigandan Ramadoss[1*], Hesheng Yu[1], Anand Rajkamal[2], Gun Jin Yun[2, 3] Ziheng Zhang[1], Chen gtao Yang[1*], Fei Ma[1], Yu Wu[1], Chen Daiqian[1], and Yuanfu Chen[1,4*]

[1]Yangtze Delta Region Institute (Huzhou), University of Electronic Science and Technology of China, Huzhou 313001, China

[2]Institute of Advanced Aerospace Technology, Seoul National University, Gwanak-gu Gwanak-ro 1, Seoul 08826, Republic of Korea

[3]Department of Aerospace Engineering, Seoul National University, Gwanak-gu Gwanak-ro 1, Seoul 08826, Republic of Korea

[4]School of Integrated Circuit Science and Engineering, State Key Laboratory of Electronic Thin Films and Integrated Devices, University of Electronic Science and Technology of China, Chengdu 610054, China

KEYWORDS: Zinc–air batteries; Iron carbon; Triple doping; Carbon nanotubes; Oxygen reduction reaction.

S1. Preparation of different modified working electrodes (GCE, RDE, RRDE, NF and air cathodes)

GCE, RDE, RRDE, NF and air cathodes were prepared with reference to the reports in the literatures[S1-S31] RDE, RRDE, GCE was first polished using alumina slurries (0.3 and 0.05 micron-sized), nickel foams and carbon clothes were consecutively acid washed, and then treated by successive ultrasonic cleaning using absolute deionized water, and ethanol. The activated electrodes were modified with the electrocatalysts ink dispersion. The 4 $mg \cdot mL^{-1}$ electrocatalyst ink was used to drop-cast onto the electrodes surface. Accordingly, a mixture of 4 mg electrocatalyst powder, ethanol (300 μL), deionized water (650 μL), and 5 wt% Nafion solution (50 μL) was ultra-sonicated for 30 min. Hence, the electrocatalyst loading on electrode surface was controlled at 0.0142 mg/cm^2 and essentially each modification was dried in air. All the experiments were demonstrated in KOH alkaline media, such as 0.1 M, 1M and 6M+0.5M ZnOAc for ORR, OER and ZAB respectively. In a typical procedure, all the calculations such as, Koutecky-Levich (K-L) for electron transfer number, hydrogen peroxide % calculation, and were mentioned in Supporting informations (S.I.) Herein, the glassy carbon electrodes (GCE) with d= 2.4 mm was working electrode, and the carbon rod was counter electrode for OER and reference electrode (saturated mercury oxide electrode (Hg/HgO)) was same for both OER and ORR; in this, Pt/C and Fe_{SAs}-PFN-CNTs modified nickel foam electrodes were used for OWS. Overall, intrinsic catalytic response, electro-kinetics, interference measurement, electron/mass transfer analysis and charging-discharging of the electrocatalysts were investigated using various electroanalytical techniques (Cyclic/linear sweep Voltammograms (CV/LSV), electrochemical impedance spectroscopy

(EIS), Chronoamperometric I-T test, open circuit potential (OCP) and chronopotentiometry (CP) and discussed in brief.

Crystallite domain size calculations

$$\text{Crystallite domain size} = (2.4 \times 10^{-10}) \frac{\lambda 4}{\left(\frac{I_D}{I_G}\right)}$$

Where, $\lambda = 532$ nm (the laser wavelength), and ID/IG is the disorder decree of D and G bands.

S2. Electrochemical characterizations

Electrochemical ORR measurements were carried out in O_2- and N_2-saturated 0.1 M KOH by using an electrochemical workstation (Pine, WaveDriver20) equipped with three electrodes. Wherein the catalyst-loaded rotating disc electrode (RDE, Pine, 5 mm; for CV, LSV, CSCA, CV cycling, *i-t*, and methanol poisoning) and a rotating-ring disc electrode (RRDE, Pine, N = 0.37; for electron transfer number and H_2O_2 yield) were used as working electrodes, while the Hg/HgO electrode and Pt wire were used as the reference and counter electrodes, respectively.

Working electrodes were prepared by sonicating 5 mg of catalyst powder in 1 mL of mixed solvents (V_{water} : $V_{ethanol}$ = 3: 1) for 5 minutes. To which, 50 µL of Nafion ink was injected and ultrasonicated for an additional 30 min. afterwards, 15 µL of catalyst ink was loaded on RDE and RRDE. The loading amounts of all the catalysts, including 20 wt. % Pt/C for ORR, were 0.29 mg cm^{-2}. All measured potentials were corrected versus the reversible hydrogen electrode (RHE) using the Nernst equation ($E_{RHE} = E_{(Hg/HgO)} + 0.0591 \times pH + 0.098$). The cyclic voltammetry (CV) curves were detected from 0.2 to 1.0 V on RDE (50 mV s^{-1}). The linear sweep voltammetry (LSV) curves were investigated from 0.2 to 1.1 V (10 mV s^{-1}, 400-2500 rpm). Cyclic step chronoamperometry (CSCA) was conducted to measure the solution resistance by adding an instantaneous 50 mV step

potential at 8 ms. The final LSV data was obtained by subtracting the background current measured in N_2-saturated electrolyte and performing *iR* compensation using the CSCA results. The CV cycling tests were carried out from 0.6 to 1.0 V for continuous 3,000 cycles (100 mV s^{-1}). The long-term durability experiments were executed by a chronoamperometry test on RDE at 0.6 V for 6 h (at 1600 rpm). Methanol tolerance tests were carried out by adding 20 mL of methanol to 90 mL of 0.1 M KOH electrolyte for Fe_{SAs}-PFN-CNTs, while 5 mL of methanol was added to 90 mL of 0.1 M KOH for commercial Pt/C.

The H_2O_2 yield and '*n*' were further detected on RRDE. The LSV was obtained from 1.1 to 0.1 V (5 mV s^{-1}, 1600 rpm). And its ring potential was set at 1.3 V. Used the subsequent equations to calculate their specific values:

$$H_2O_2(\%) = 200 \times \frac{\frac{I_r}{N}}{I_d + \frac{I_r}{N}}$$

$$n = 4 \times \frac{I_d}{I_d + \frac{I_r}{N}}$$

Wherein, I_r: ring current; I_d: disk current; N: collection efficiency of the Pt ring (N = 0.37).

The Koutecky–Levich equation was provided to evaluate the values of electron transfer number (*n*).

$$\frac{1}{j} = \frac{1}{j_d} + \frac{1}{j_k} = \frac{1}{B\omega^{1/2}} + \frac{1}{j_k}$$

$$B = 0.2nFC_0D^{2/3}V^{-1/6}$$

Wherein, j: measured current density; j_K: kinetic current density; j_d: diffusion-limited current density; ω: the angular velocity of the disk (rad s^{-1}); F: Faraday constant (96485 C mol^{-1}); C_0: bulk

concentration of O_2 (1.2×10^{-6} mol cm^{-3}); D_0: diffusion coefficient of O_2 in 0.1 M KOH (1.9×10^{-5} cm^2 s^{-1}); V: kinematic viscosity of the electrolyte (0.01 cm^2 s^{-1}).

Similarly, the same catalyst ink was loaded (5 μL) on a glassy carbon working electrode (GCE; 3 mm diameter) to evaluate the OER performance tests on a CHI 660D electrochemical workstation in 0.1 M KOH. The reference RuO_2 catalyst ink was also prepared in the same manner and loaded on polished GCE (5 μL on 3 mm GCE; loading amount was 0.26 mg cm^{-2}). Herein, the three-electrode system is assembled by a catalyst-loaded GCE working electrode, a graphite counter electrode, and a Hg/HgO reference electrode. LSV curves were acquired by scanning the potential from 0 to 0.8 V versus the Hg/HgO electrode with a scanning speed of 5 mV s^{-1}. The electrochemical impedance spectroscopy (EIS) tests were performed from 0.1 to 100 kHz. CV cycling was carried out using catalysts modified GCE and the *i-t* tests were performed on nickel foam current collectors (2 cm x 1 cm; catalyst loading was 1 mg cm^{-2}).

A Zn-O_2 battery was constructed in a 6 M KOH aqueous electrolyte consisting of 0.5 M $Zn(Ac)_2$ using a CHI 660D electrochemical workstation. Polished zinc sheet was used as a metal anode (thickness of 0.3 mm), and the bifunctional electrocatalyst-loaded carbon paper was employed as air cathode. Electrocatalyst ink preparation is the same as above, and the obtained homogeneous link was loaded on carbon paper and dried in a 50 ºC electric oven before assembling the Zn-air battery. While Pt/C-RuO_2 mixed catalyst ink was also prepared in the same method by dispersing 5 mg of both catalysts (1:1 wt.%) in a mixed solution of 750 μL of water, 250 μL of deionized water, and 50 μL of Nafion ink by ultrasonication for 30 min. The homogenous ink was dropped onto the carbon paper, and the mass loading of the catalysts was 1.5 mg cm^{-2}. All the electrochemical data of the as-prepared electrocatalysts presented in this article has been tested twice to make sure all the results are reliable and reproducible.

Table S1: Bifunctional_activity of Fe_{SAs}-PFN-CNTs performance and other compared transition-metal-based materials

Activities / Materials	η@10 mA/cm^2	Tafel slope (mV/ dec)	Electrolyte	Ref.
Co_9S_8/CD@NSC	390 mV	113	1.0 M KOH	S2
Co, N, P-PCNS	319 mV	91.1	1.0 M KOH	S19
Co@CoO_x	289 mV	68.9	1.0 M KOH	S20
Co2P@NCNT	470mV	35.49	1.0 M KOH	S21
Co@CoO_x/*N-C*	322 mV	73.3	1.0 M KOH	S22
SS-Co-SAC NSAs	348 mV	94.2	1.0 M KOH	S23
Co-Ni-Se/C	290 mV	143	1.0 M KOH	S24
Co@NCNTs	351 mV	180.7	1.0 M KOH	S25
$NiSe_2/C_3N_4$	300 mV	58	1.0 M KOH	S26
CoNi-OCNC	346 mV	67	1.0 M KOH	S27
Fe_{SAs}-PFN-CNTs	**310 mV**	**63.8**	**1.0 M KOH**	**This work**

Table S2: ORR performance of Fe_{SAs}-PFN-CNTs in comparison with few more synthesized catalysts in 0.1 M KOH solution.

Activities / Materials	E_{onset} (V)	$E_{1/2}$ (V)	J_d at 0.6 V (mA cm^{-2})	Jk at 0.8 V (mA cm^{-2})
PFN-CNT	0. 87	0.815	*3.89*	2.4
Fe@P-CNT	0.95	0.82	5.15	9.6
Fe@N-CNT	0.934	0.835	*5.97*	36.3
Pt/C	0.957	0.828	*5.21*	19.4
Fe_{SAs}-PFN-CNTs	0.98	0.885	*6.32*	144.2

Table S3: ORR performance of Fe_{SAs}-PFN-CNTs in comparison with the other reported non-noble metal electrocatalysts.

Activities / Materials	Onset potential (V vs RHE)	Half-wave (E1/2) potential (V vs RHE)	*Electrolyte*	Ref.
FC@NCs-4.15	0.1 M KOH	0.94	0.1 M KOH	S1
Co9S8/ CD@NSC	0.933	0.84 V	0.1 M KOH	S2
Fe-HNC	0.93	0.85	0.1 M KOH	S3
Fe/Co @NC-WO_{2-x}	0.93	0.87	0.1 M KOH	S4
FeCo-N-HCN	0.91	0.86	0.1 M KOH	S5
Fe SAs@S/N-C	0.96	0.84	0.1 M KOH	S6
Fe-N-C-S	0.99	0.90	0.1 M KOH	S7
Fe-N/P-C-700	0.941	0.867	0.1 M KOH	S8
NPS-G-2	0.96	0.85	0.1 M KOH	S9
Fe/OES	1.0	0.85	0.1 M KOH	S10
CoFe-CB	/	0.86	0.1 M KOH	S11
Fe@SNDC–950	0.98	0.83	0.1 M KOH	S12
NSCHCT1000	1.02	0.84	0.1 M KOH	S13
Fe-N-DSC	1.03	0.84	0.1 M KOH	S14
Co_{NP}/Co_{SA}-N-C	0.95	0.83	0.1 M KOH	S15
Co-N-PCNF	0.95	0.81	0.1 M KOH	S16
Fe-Co-N-C-900	0.97	0.86	0.1 M KOH	S17
Fe/Mn-NIHPC	0.95	0.86	0.1 M KOH	S18
Fe_{SAs}-PFN-CNTs	**0.98**	**0.885**	**0.1 M KOH**	**This work**

Table S4. Comparison of the performance of Fe_{SAs}-PFN-CNTs based Zn-Air battery with other reported electrocatalysts.

Activities / Materials	Open-circuit voltage (V)	Maximum power density (mW cm^{-2})	Specific capacity (mAh g^{-1}) @J (mA cm^{-2})	Ref.
Co9S8/CD@NSC	-	92.7	-	S2
Fe $_{SAs}$@S/N-C	1.51	156	794@10	S6
Fe-N-C-S	1.49	201	854@10	S7
Fe-N/P-C	1.42	133.2	723.6@100	S8
NPS-G-2	1.372	151	686@10	S9
Fe/OES	1.5	186.8	807.5@5	S10
FeCo/NC	1.472	130	725.6@10	S15
Co,N,P-PCNS	1.498	101.3	-	S19
FeCo@HOMNCP	1.619	134	786.5@10	S28
FeMn-DSAC	1.45	181	734@2	S29
Co/Co_9S_8-NCL-30	1.485	112	674@10	S30
Fe_{NP}@Fe-N-C	1.45	106.5	711@10	S31
FeP/NPC-DNA	1.394	111.2	789.4@10	S32
NP-Co_{SA}NC	1.42	158.1	768.4@20	S33
Fe_{SAs}-PFN-CNTs	**1.49**	**241**	**781@20**	**This work**

S2. Characterizations

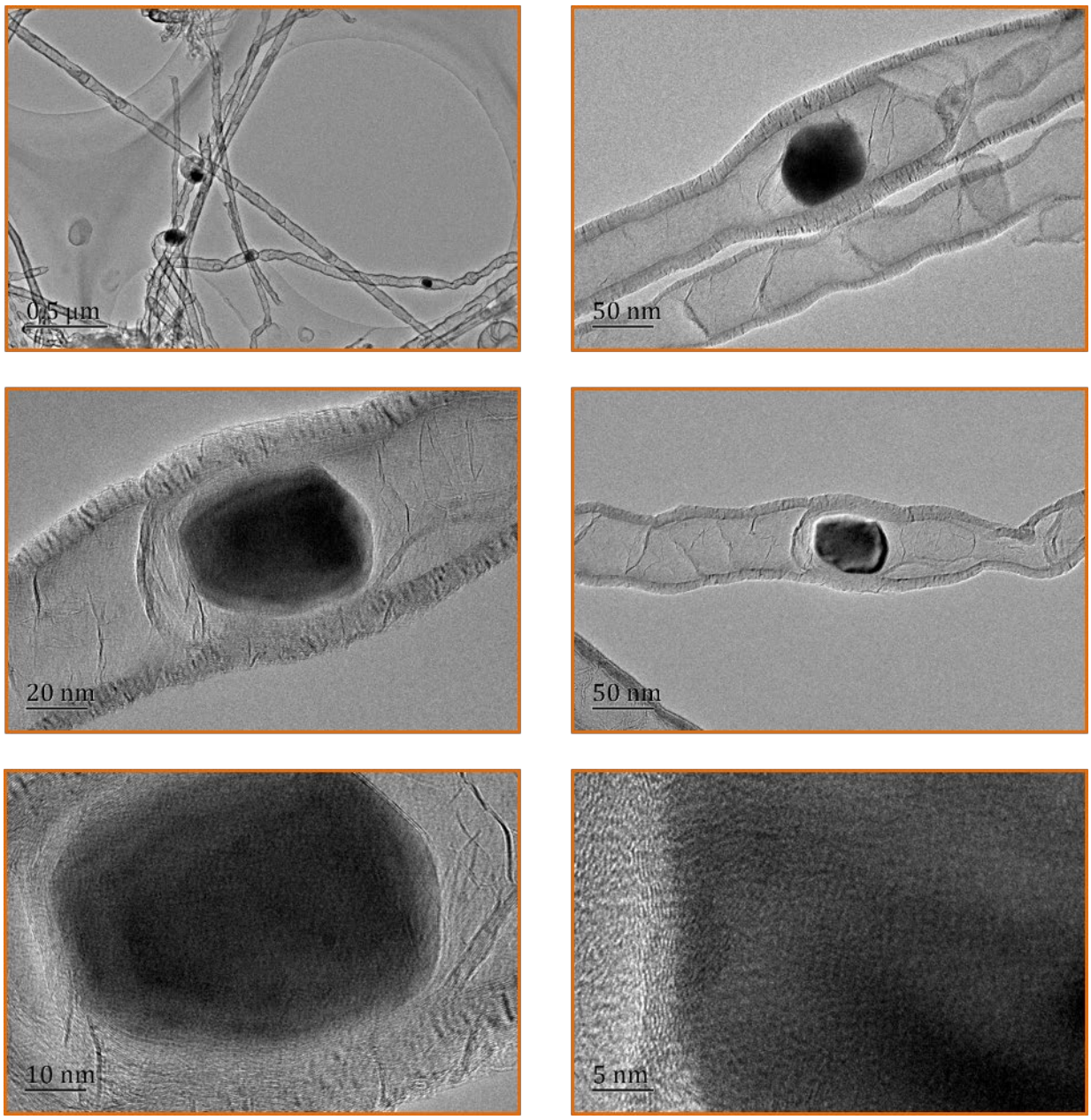

Fig S1. Additional HRTEM images

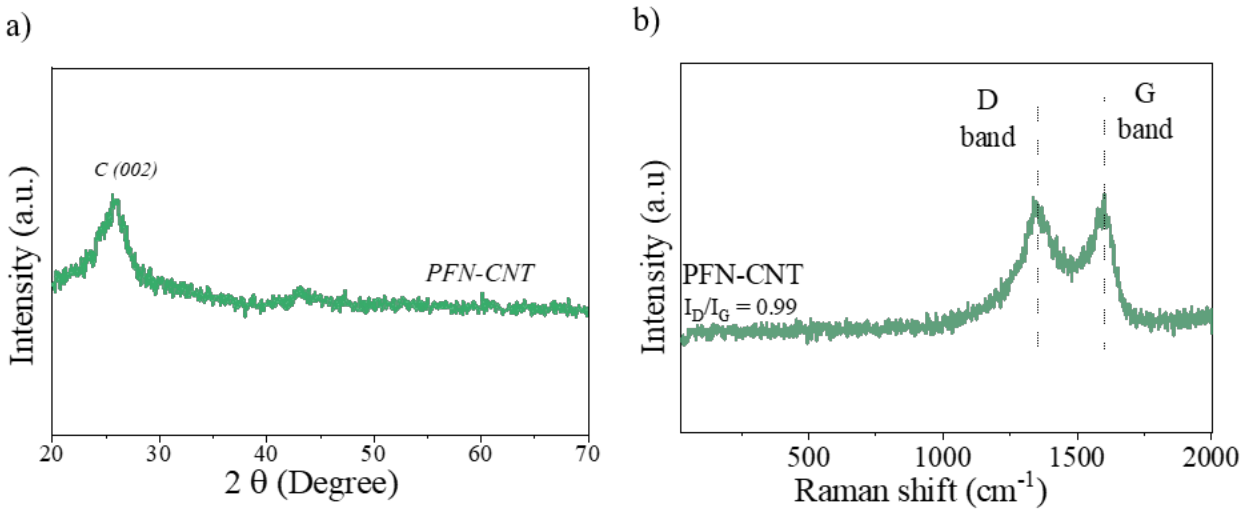

Fig. S2 XRD pattern of PFN-CNT, b) Raman spectrum of PFN-CNT

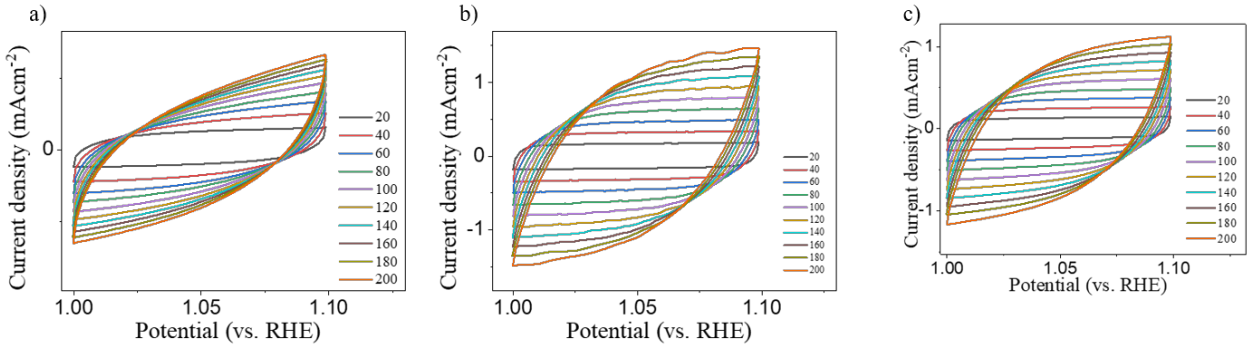

Fig. S3. (a-d) The plots of cyclic voltammograms operated in a non-Faradaic capacitive current range to estimate the ECSA in 0.1 M KOH electrolyte.

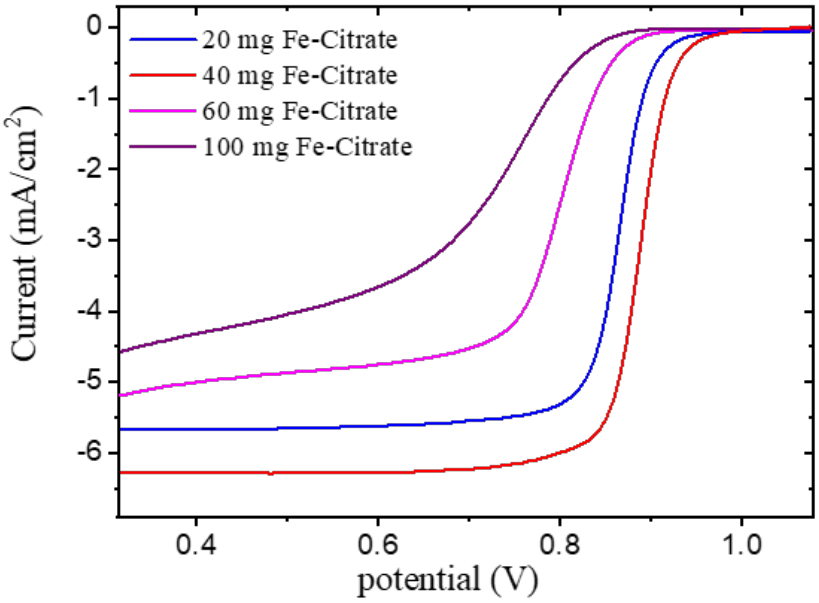

Fig. S4. LSV curves of Fe_{SAs}-PFN-CNTs with different iron citrate loading amount in presence of O_2 purging

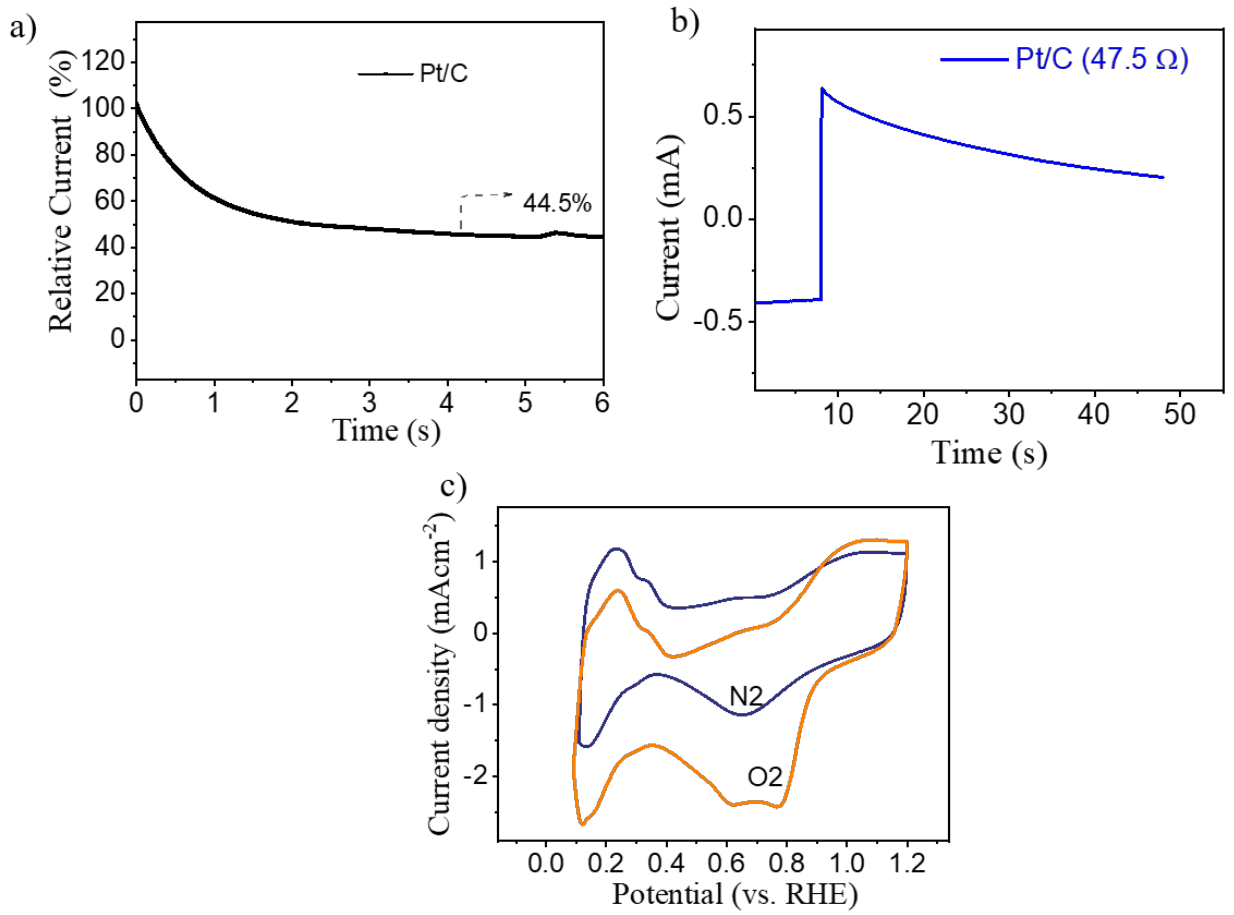

Fig. S5. I-T stability test and, b) CSCA plot obtained for Pt/C in O_2-saturated and c) CV plots obtained for commercial Pt/C in N_2- and O_2-saturated 0.1 M KOH.

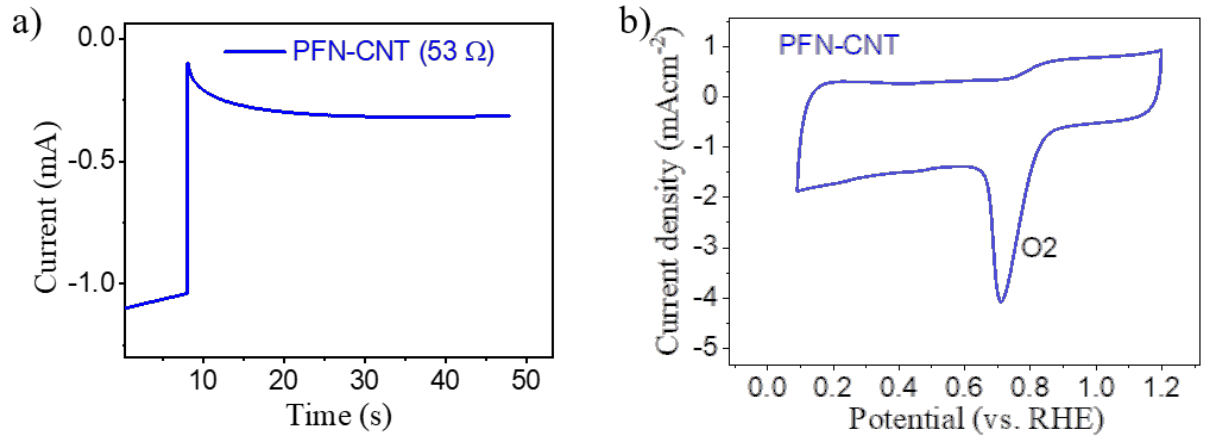

Fig. S6. (a) CSCA plot and (b) CV plot obtained for PFN-CNTs in O_2-saturated 0.1 M KOH.

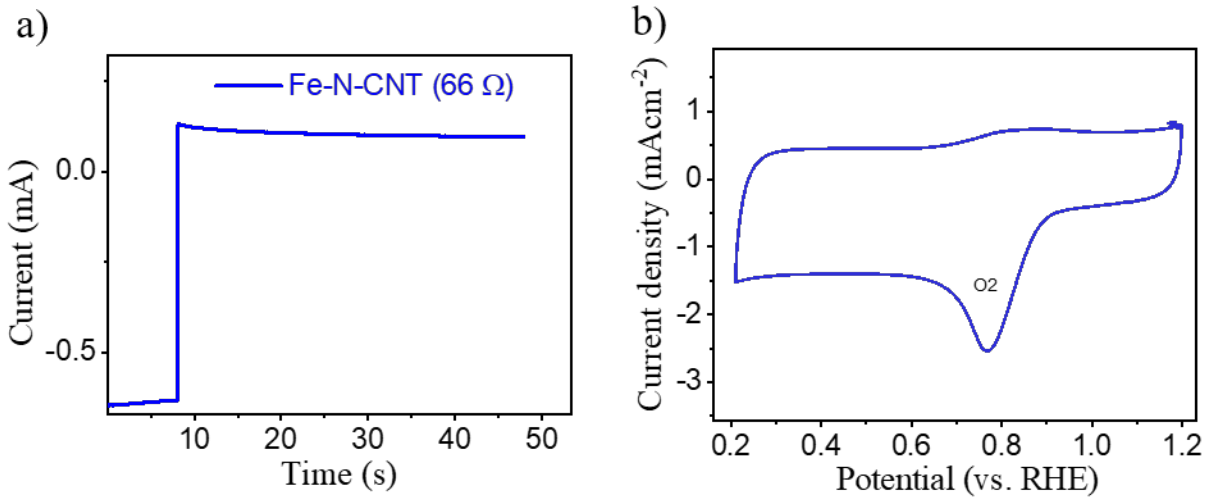

Fig. S7. (a) CSCA plot and (b) CV plot obtained for Fe-N-CNTs in O_2-saturated 0.1 M KOH.

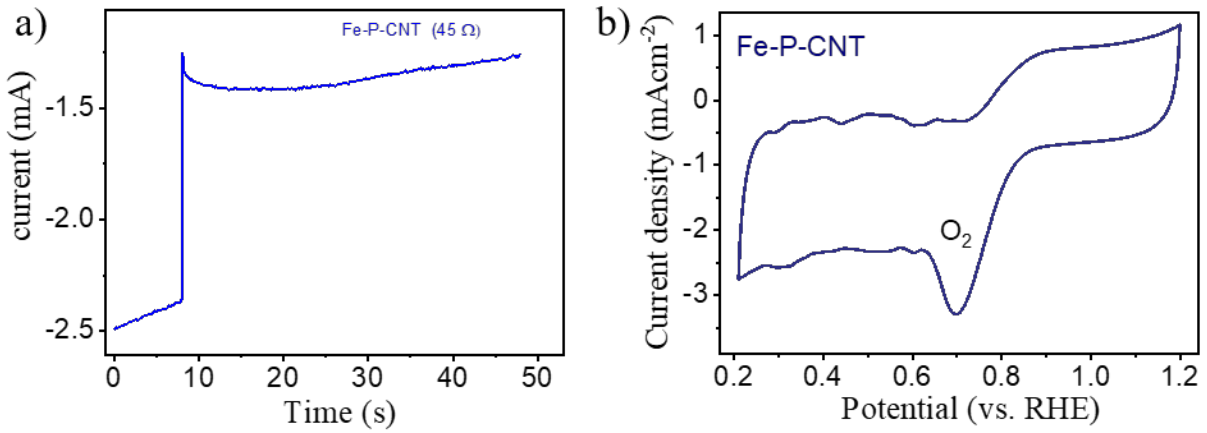

Fig. S8. (a) CSCA plot and (b) CV plot obtained for Fe-P-CNTs in O_2-saturated 0.1 M KOH.

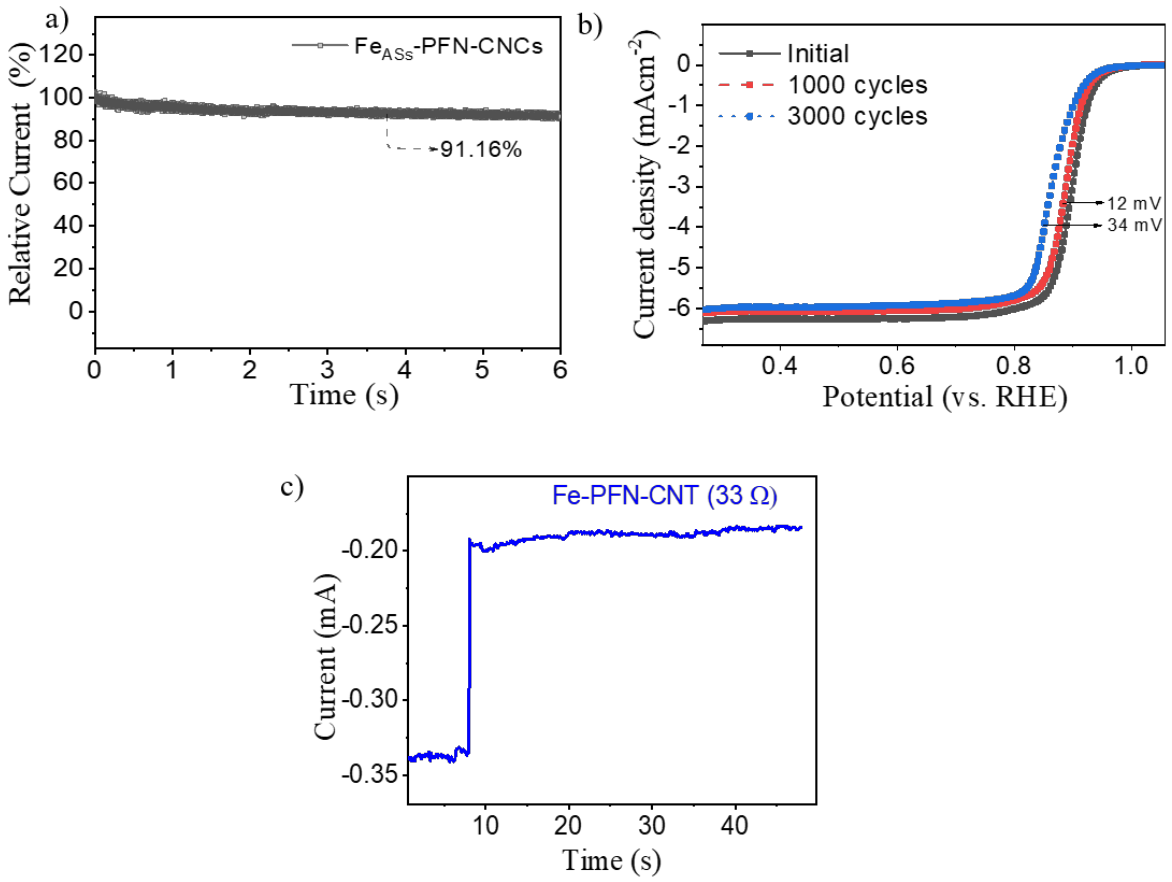

Fig. S9. (a) I-T stability test and (b) cycling stability obtained using LSV plot at initial and after 1000 and 3000 cycles, respectively and c) CCSA study of Fe$_{SAs}$-PFN-CNTs in O_2-saturated 0.1 M KOH.

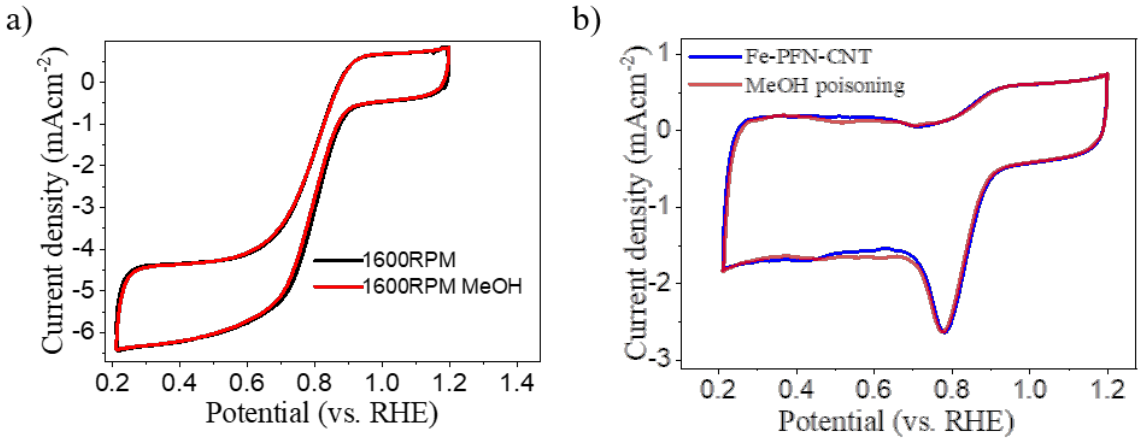

Fig. S10. (a) Methanol poisoning test obtained using CV plot for Fe$_{SAs}$-PFN-CNTs in O_2-saturated 0.1 M KOH in presence and absence of stirring a) 1600 rpm B) no stirring.

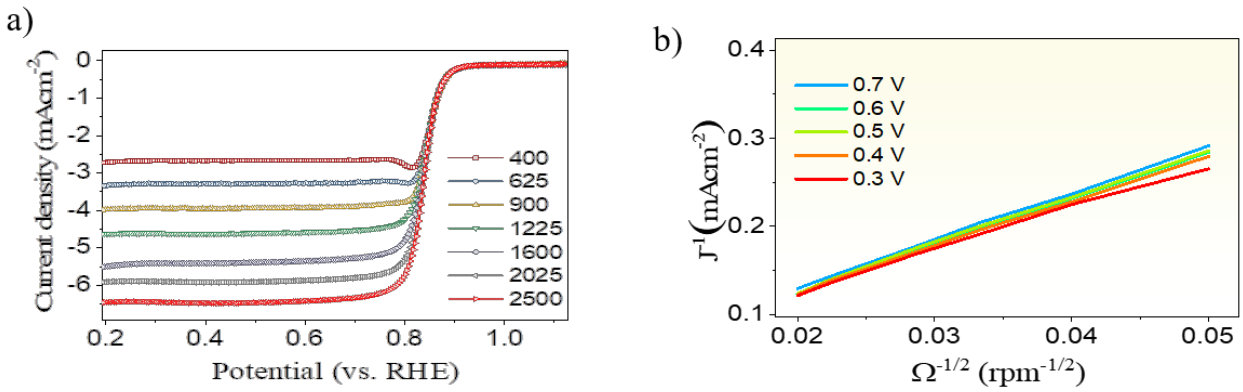

Fig. S11. (a) LSV plots obtained by varying the rotation speed from 400-2500 rotations per minute (RPM) for Fe-N-CNT, and (b) the corresponding Koutecky–Levich (K–L) plots.

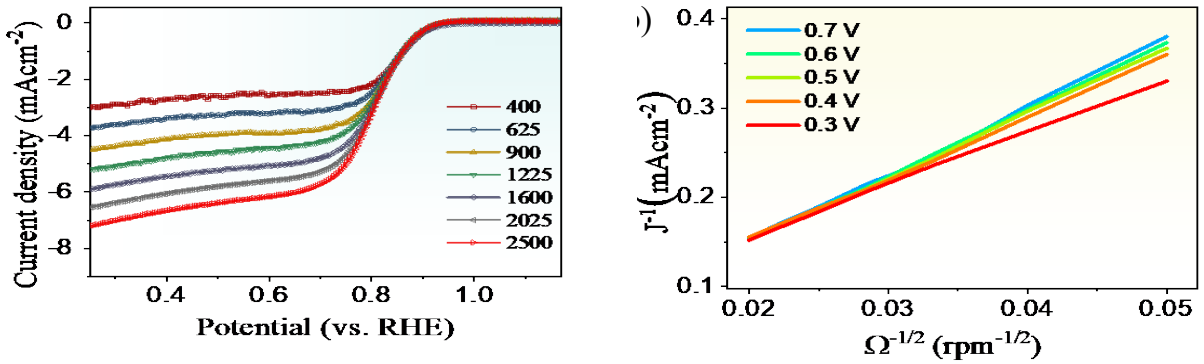

Fig. S12. (a) LSV plots obtained by varying the rotation speed from 400-2500 rotations per minute (RPM) for Fe-P-CNT, and (b) the corresponding Koutecky–Levich (K–L) plots.

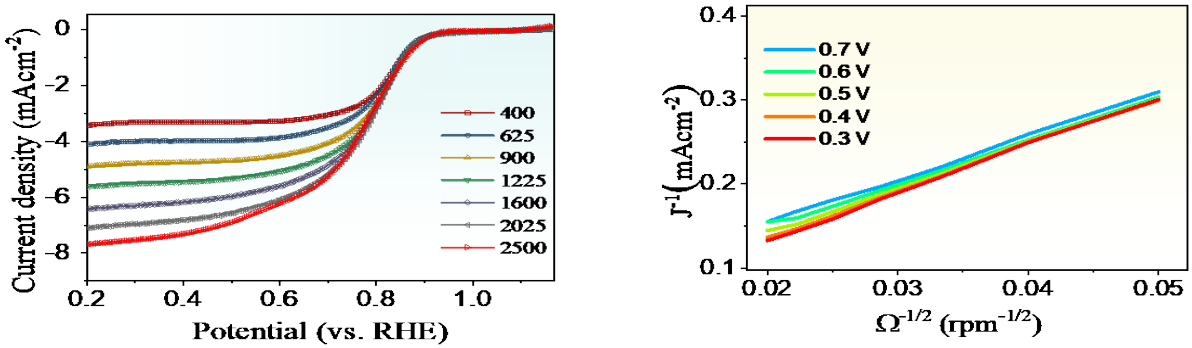

Fig. S13. (a) LSV plots obtained by varying the rotation speed from 400-2500 rotations per minute (RPM) for commercial Pt/C, and (b) the corresponding Koutecky–Levich (K–L) plots.

S3. Computational details

All calculations are performed in the Vienna Ab-initio Simulation Package (VASP) using spin polarized density functional theory[34]. Projected Augmented Wave (PAW) method is used to describe the potentials of the atoms with Generalized Gradient Approximation (GGA) is considered for exchange and correlation effects at Perdew-Burke-Ernzerhof (PBE) level[35]. Grimme's correction is used with PBE for Van der Waal's correction[36]. Plane wave cut-off energy of 450 eV is used for the calculations. $3 \times 1 \times 1$ K-point grid is used for the brillouin zone sampling with Monkhorst Pack scheme. Structural optimizations were done until the total energy converged less than 10^{-5} eV per atom and the maximum force converged less than 0.02 eV/Å.

S3.1. Modelling

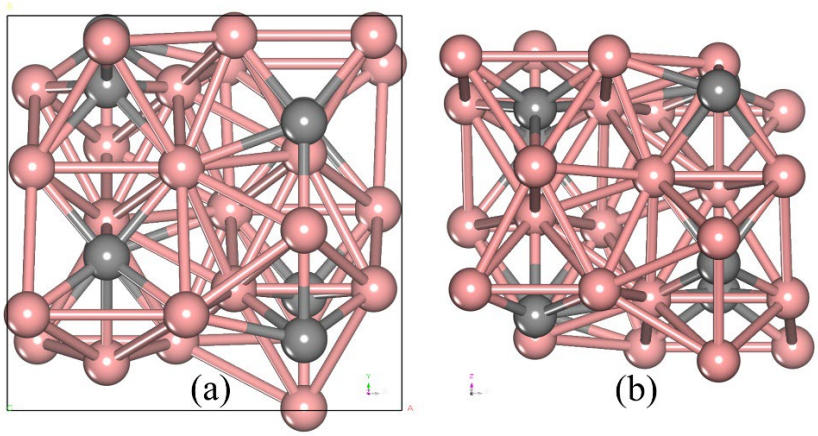

Fig. S14. Structure of Fe_3C with (110) crystal face constructed on CNT for theoretical calculation in this work.

To construct the Fe active site model, a (8,8) carbon nanotube (CNT) was used in a 1×5 supercell. The computational models were optimized with cell dimensions of a = 12.12 Å, b = 24.187 Å, c = 30 Å, and lattice angles $\alpha = \beta = \gamma = 90°$.

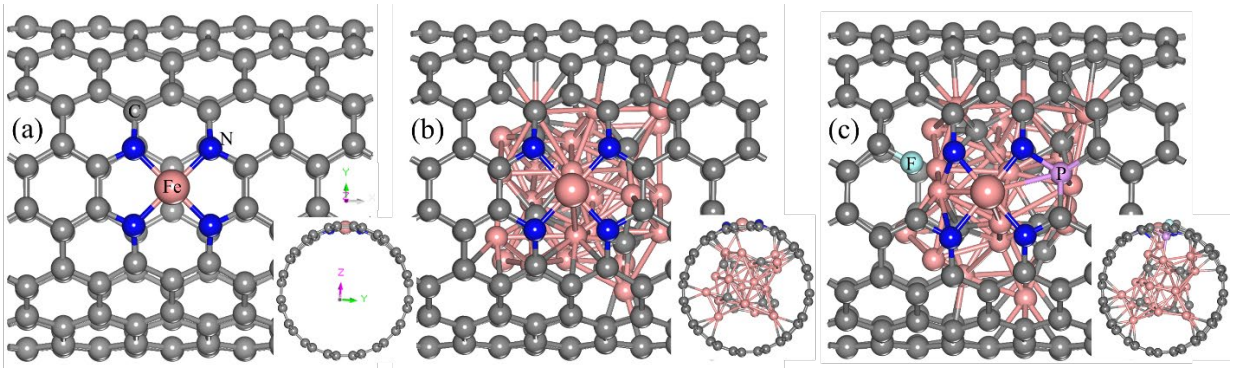

Fig. S15. Top and side view of an optimized structures of (a) Fe-N_4CNT. (b) Fe_3C-Fe-N_4-CNT (Fe_{SAs}-N-CNTs). (c) Fe_3C-PF-Fe-N_4-CNT (Fe_{SAs}-PFN-CNTs).

A vacuum of 15 Å was introduced along the z-axis to prevent any unintended interactions between the periodic images. Three distinct configurations were considered: (i) FeN_4 supported on carbon nanotubes (Fe-N_4CNT), (ii) Fe_3C embedded in the CNT structure with its (110) lattice plane (see **Fig.S14**) exposed to FeN_4 active sites (Fe_{SAs}-N-CNTs), and (iii) a similar Fe_3C insertion with phosphorus (P) and fluorine (F) dopants in the FeN_4-CNT matrix (Fe_{SAs}-PFN-CNTs). Optimized structures for each configuration are illustrated in **Fig. 15a-c, 16**.

S3.2. Steps for Oxygen Evolution Reaction (OER):

$$\mathbf{\Delta G_1} = * + 4OH^- \rightarrow OH^* + 3OH^- + e^- \quad (1)$$

Surface reacts with hydroxide ions to form surface-bound hydroxyl species (OH) and releases one electron.

$$\mathbf{\Delta G_2} = OH^* + 3OH^- + e^- \rightarrow O^* + H_2O + 2OH^- + 2\,e^- \quad (2)$$

Surface-bound OH* reacts, releasing water and forming surface-bound oxygen (O*).

$$\mathbf{\Delta G_3} = O^* + 2OH^- + H_2O + 2e^- \rightarrow OOH^* + H_2O + OH^- + 3e^- \quad (3)$$

O* reacts with hydroxide ions to form surface-bound peroxide species (OOH*).

$$\mathbf{\Delta G_4} = OOH^* + H_2O + OH^- + 3e^- \rightarrow O_2 + 2H_2O + 4e^- \quad (4)$$

OOH* releases oxygen gas (O_2) and additional water.

S3.3. Steps for Oxygen Reduction Reaction (ORR):

$$\mathbf{\Delta G_1} = O_2 + 2H_2O + 4e^- \rightarrow OOH^* + H_2O + OH^- + 3e^- \quad (5)$$

Oxygen gas reacts with water to form surface-bound peroxide (OOH*).

$$\mathbf{\Delta G_2} = OOH^* + H_2O + OH^- + 3e^- \rightarrow O^* + 2OH^- + H_2O + 2e^- \quad (6)$$

Surface-bound peroxide reacts to form surface-bound oxygen (O*).

$$\mathbf{\Delta G_3} = O^* + 2OH^- + H_2O + 2e^- \rightarrow OH^* + 3OH^- + e^- \quad (7)$$

Surface-bound oxygen reacts to form surface-bound hydroxyl (OH*).

$$\mathbf{\Delta G_4} = OH^* + 3OH^- + e^- \rightarrow * + 4OH^- \quad (8)$$

Surface-bound hydroxyl returns to the initial state, completing the ORR cycle.

Free energy difference ΔG is calculated by following [37],

$$\Delta G = \Delta E_{DFT} + \Delta ZPE - T\Delta S - neU \quad (9)$$

* denotes the active site on a surface, while molecules marked with * represent those in an adsorbed state. The terms E_{DFT} and ZPE refer to the total energy from DFT calculations and the zero-point energy of free molecules, respectively. The variables TS, n, and U represent the entropy obtained from vibrational frequency calculations, the number of electrons transferred, and the applied potential on the electrode, respectively. At the equilibrium potential of U = 0.4 V, the potential-determining step (PDS) is the one with the highest uphill energy difference in the free energy profile, from which the overpotential (η) is calculated for the active site. A lower overpotential indicates a more efficient site.

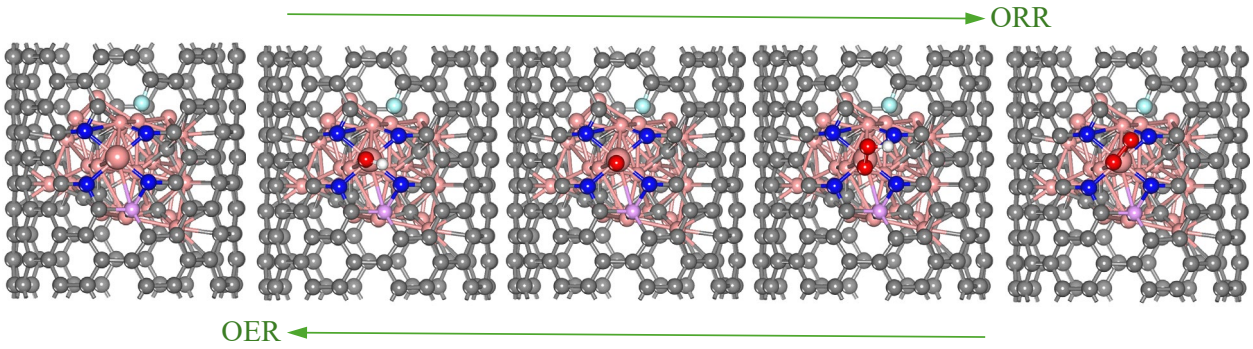

Fig. S16. Optimized structures of the ORR and OER intermediates on Fe_{SAs}-PFN-CNTs.

S3.4. *d*-band center

The *d*-band center is calculated using formula

$$d\text{-band center} = \frac{\int_{-\infty}^{0} \rho_d E \, dE}{\int_{-\infty}^{0} \rho_d dE} \quad (10)$$

Here, ρ is depicted as the density of d and E is depicted as the energy eigen value.

S4. DFT studies: Results and discussion

First-principles Density Functional Theory (DFT) calculations were carried out to investigate the roles of phosphorus (P), iron (Fe), and iron carbide (Fe_3C) species in enhancing the bifunctional oxygen reduction reaction (ORR) and oxygen evolution reaction (OER) activities within the Fe-N_4-CNT structure. It is widely recognized that transition metal centers in single-atom catalysts (SACs) often exhibit strong binding to O_2 molecules, coupled with high energy barriers for the four-electron ORR and OER processes. This results in suboptimal bifunctional catalytic activity. However, based on electrocatalytic experiments, it was anticipated that the introduction of Fe_3C at the interface would reduce the energy barriers for both ORR and OER on Fe_{SAs}-PFN-CNTs active sites, potentially improving their overall performance.

The *d*-band center, a key descriptor for the catalytic activity of metal atoms, was calculated using eq 10[38,39]. In comparison to the Fe–N_4–CNT system, where the d-band center of Fe is -2.63 eV, the values shift upward to -2.12 eV in the Fe_{SAs}-N-CNTs system and -2.31 eV in the Fe_{SAs}-PFN-CNTs system (**Fig. S17**). This shift indicates that the incorporation of Fe_3C, along with phosphorus (P) and fluorine (F) dopants, modifies the electronic structure of the Fe atoms, promoting more favourable O_2 adsorption and thereby enhancing bifunctional catalytic activity.

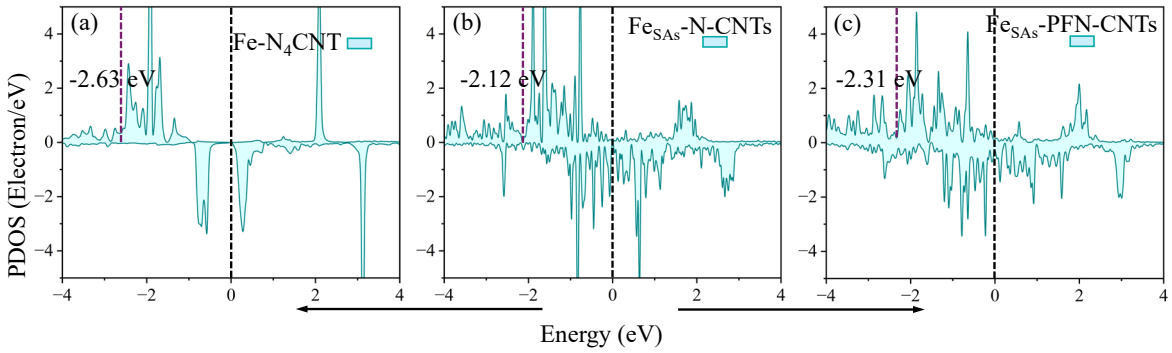

Fig. S17. Projected density of states (PDOS) of Fe *d*-band in (a) Fe-N_4-CNT (b) Fe_3C-Fe-N_4-CNT (Fe_{SAs}-N-CNTs) and (c) Fe_3C-PF-Fe-N_4-CNT (Fe_{SAs}-PFN-CNTs).

From the **Fig. S18**, the O_2→*OOH step in Fe-N_4-CNT requires overcoming a 0.19 eV energy barrier, which hinders smooth oxygen activation. Similarly, the *OH→*O step in OER requires a higher energy barrier of 0.86 eV. Upon integrating Fe_3C into the Fe-N_4-CNT, the ORR barrier is significantly reduced to 0.02 eV, improving the ORR activity. However, the OER step requires a much higher energy barrier of 1.18 eV, indicating a less favorable condition for OER activity. In contrast, when Fe_3C is integrated into the Fe_{SAs}-PFN-CNTs structure, the ORR and OER performance becomes more balanced. The ORR energy barrier is lowered to 0.11 eV, and the OER barrier is reduced to 0.53 eV, making it more optimal for dual-function catalytic activity. These findings highlight that Fe_3C, P and F integration can significantly enhance the ORR/OER performance of single-atom Fe-based catalysts, especially in improving both ORR and OER activities.

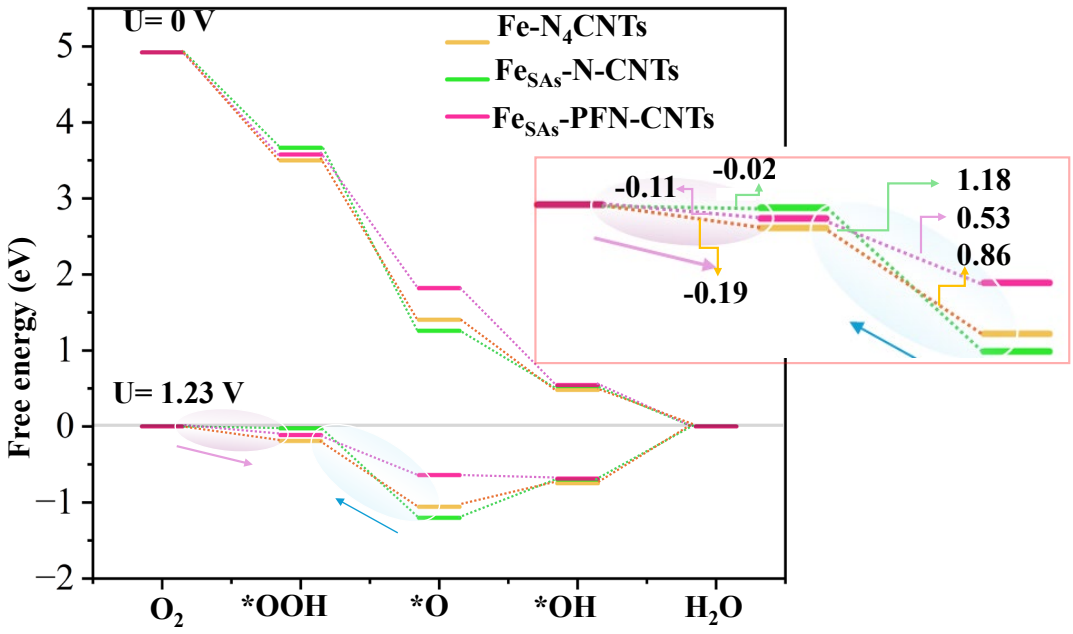

Fig. S18. Gibbs free energy changes of ORR and OER on Fe-N4-CNT, Fe3C-Fe-N4-CNT and Fe3C-PF-Fe-N4-CNT.

To understand these changes in the energy barrier, we studied the bader charge calculations. **Fig. S19** shows the Bader charge transfer analysis for three systems, Fe-N4CNT, FeSAs-N-CNTs and FeSAs-PFN-CNTs systems. The bader charge for Fe in the FeSAs-PFN-CNTs, the electron-rich Fe3C serves as an electron donor, transferring 0.066 (see **Fig. S19a**) electrons to the electron-withdrawing Fe–N4–CNT site which is agrees with previous report[40]. This electron donation results in a decrease in the Fe (+*ve*) charge value from 0.948 to 0.882*e*. In case of FeSAs-PFN-CNTs, the charge transfer is 0.141*e* (see **Fig. S19b**). This electron donation results in a decrease in the Fe (+*ve*) charge value from 1.092*e* to 0.951*e*. Hence, Upon incorporating PF into the Fe–N4–CNT system, our calculations reveal an increase in the Fe charge value to 1.092*e*, indicating that P and F functions as an electron donor (0.073e) and acceptor (0.217), from the Fe center (see **Fig. S19c**). When both P and F and Fe3C are introduced into the Fe–N4–CNT system, the charge on the Fe site stabilizes at 0.95*e*, suggesting a compensatory effect between the electron-donating Fe3C and the electron-accepting P and F. This dual modulation of charge density-electron donation from Fe3C and electron withdrawal by P and F-likely plays a crucial role in regulating the adsorption and desorption of oxygen-related intermediates on the Fe–N4CNT catalytic sites. This modulation enhances the catalytic efficiency by facilitating reversible ORR and OER, making the system a promising candidate for applications in energy conversion technologies.

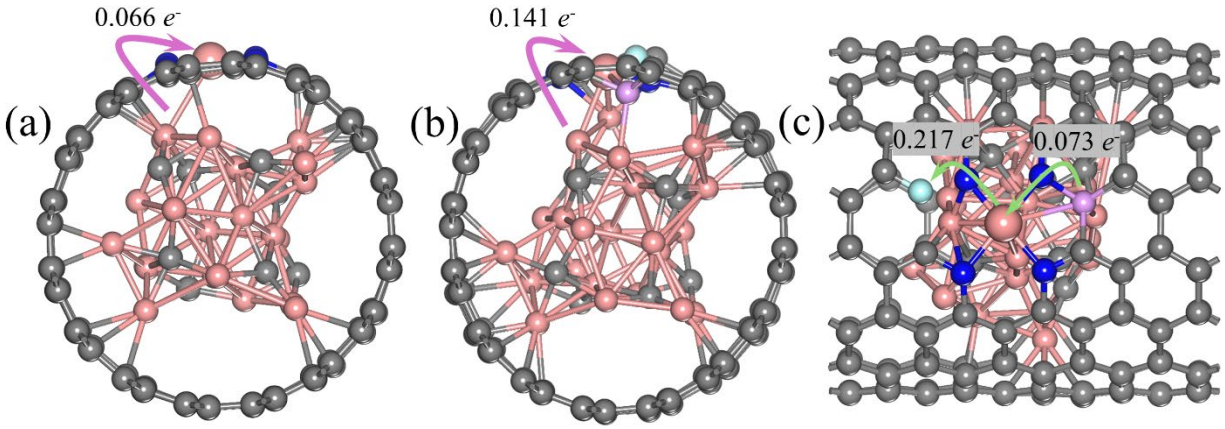

Fig. S19. Bader charge transfer analysis for e- transfer in the (a) Fe_3C-Fe-N_4-C, (b) side and (c) top view of Fe_3C-PF-Fe-N-C system.

References

1. X. Luo, H. Ma, H. Ren, X. Zou, Y. Wang, X. Li, Z. Shen, Y. Wang, L. Cui, Controllable synthesis of nitrogen-doped carbon containing Co and Co3Fe7 nanoparticles as effective catalysts for electrochemical oxygen conversion, J. Colloid Interface Sci. 590 (2021) 622-631, https://doi.org/10.1016/j.jcis.2021.01.097.
2. Zhang, P.; Bin, D.; Wei, J.-S.; Niu, X.-Q.; Chen, X.-B.; Xia, Y.-Y.; Xiong, H.-M. Efficient Oxygen Electrocatalyst for Zn–Air Batteries: Carbon Dots and Co9S8 Nanoparticles in a N,S-Codoped Carbon Matrix. ACS Applied Materials & Interfaces 2019, 11 (15), 14085. DOI: 10.1021/acsami.8b22557
3. X. Zhang, S. Zhang, Y. Yang, L. Wang, Z. Mu, H. Zhu, X. Zhu, H. Xing, H. Xia, B. Huang, J. Li, S. Guo, E. Wang, A General Method for Transition Metal Single Atoms Anchored on Honeycomb-Like Nitrogen-Doped Carbon Nanosheets, Adv. Mater. 32 (2020) 1906905, https://doi.org/10.1002/adma.201906905
4. Q. Han, X. Zhao, Y. Luo, L. Wu, S. Sun, J. Li, Y. Wang, G. Liu, Z. Chen, Synergistic Binary Fe-Co Nanocluster Supported on Defective Tungsten Oxide as Efficient Oxygen Reduction Electrocatalyst in Zinc-Air Battery, Adv. Sci. 9 (2022) 2104237, https://doi.org/10.1002/advs.202104237.
5. H.X. Li, Y.L. Wen, M. Jiang, Y. Yao, H.H. Zhou, Z.Y. Huang, J.W. Li, S.Q. Jiao, Y.F. Kuang, S.L. Luo, Understanding of Neighboring Fe-N4-C and Co-N4-C Dual Active Centers for Oxygen Reduction Reaction, Adv. Funct. Mater. 31 (2021) 2011289, https://doi.org/10.1002/adfm.202011289.
6. Yang, T.; Ge, B.; Liu, X.; Zhang, Z.; Chen, Y.; Liu, Y. Boosting Electrocatalytic Activity of Single Atom Iron Catalysts through Sulfur-Doping Engineering for Liquid and Flexible Rechargeable Zn-air Batteries. Journal of Materials Chemistry A 2024, DOI:10.1039/d4ta00524d 10.1039/d4ta00524d.
7. Wang, K.; Zhang, X.; Xiang, X.; Wang, Y.; Lyu, D.; Xi, S.; Tian, Z. Q. In Situ S-Doping Strategy of Promoting Iron Coordinated by Nitrogen-Doped Carbon Nanosheets for Efficient Oxygen Reduction Reaction. ACS Applied Materials & Interfaces 2022, 14 (41), 46548.
8. Yuan, K.; Lützenkirchen-Hecht, D.; Li, L.; Shuai, L.; Li, Y.; Cao, R.; Qiu, M.; Zhuang, X.; Leung, M. K. H.; Chen, Y.et al. Boosting Oxygen Reduction of Single Iron Active Sites

via Geometric and Electronic Engineering: Nitrogen and Phosphorus Dual Coordination. Journal of the American Chemical Society 2020, 142 (5), 2404.https://doi.org/10.1021/jacs.9b11852.

9. Zheng, X.; Wu, J.; Cao, X.; Abbott, J.; Jin, C.; Wang, H.; Strasser, P.; Yang, R.; Chen, X.; Wu, G. N-, P-, and S-doped graphene-like carbon catalysts derived from onium salts with enhanced oxygen chemisorption for Zn-air battery cathodes. Applied Catalysis B: Environmental 2019, 241, 442.
10. C.C. Hou, L. Zou, L. Sun, K. Zhang, Z. Liu, Y. Li, C. Li, R. Zou, J. Yu, Q. Xu, Single-Atom Iron Catalysts on Overhang-Eave Carbon Cages for High-Performance Oxygen Reduction Reaction, Angew Chem. Int. Ed. 59 (2020) 7384-7389, https://doi.org/10.1002/anie.202002665.
11. W. Zhu, Y. Pei, J.C. Douglin, J. Zhang, H. Zhao, J. Xue, Q. Wang, R. Li, Y. Qin, Y. Yin, D.R. Dekel, M.D. Guiver, Multi-scale study on bifunctional Co/Fe-N-C cathode catalyst layers with high active site density for the oxygen reduction reaction, Appl. Catal. B 299 (2021) 120656, https://doi.org/10.1016/j.apcatb.2021.120656.
12. Choudhury, F. A.; Norouzi, N.; Amir, K.; Demir, M.; El-Kaderi, H. M. Iron-based sulfur and nitrogen dual doped porous carbon as durable electrocatalysts for oxygen reduction reaction. International Journal of Hydrogen Energy 2022, 47 (9), 6078.https://doi.org/10.1016/j.ijhydene.2021.12.020
13. Z. Li, Y. Yao, Y. Niu, W. Zhang, B. Chen, X. Zeng, J. Zou, Multi-heteroatom-doped hollow carbon tubes as robust electrocatalysts for the oxygen reduction reaction, oxygen and hydrogen evolution reaction, Chem. Eng. J. 418 (2021) 129321, https://doi.org/10.1016/j.cej.2021.129321
14. Z. Huang, H. Pan, W. Yang, H. Zhou, N. Gao, C. Fu, S. Li, H. Li, Y. Kuang, In Situ Self-Template Synthesis of Fe-N-Doped Double-Shelled Hollow Carbon Microspheres for Oxygen Reduction Reaction, ACS Nano 12 (2018) 208-216, https://doi.org/10.1021/acsnano.7b05832.
15. X. Cheng, J. Yang, W. Yan, Y. Han, X. Qu, S. Yin, C. Chen, R. Ji, Y. Li, G. Li, G. Li, Y. Jiang, S. Sun, Nano-geometric deformation and synergistic Co nanoparticles Co-N4 composite sites for proton exchange membrane fuel cells, Energy Environ. Sci. 14 (2021) 5958-5967, https://doi.org/10.1039/d1ee01715b.

16. Y. He, H. Guo, S. Hwang, X. Yang, Z. He, J. Braaten, S. Karakalos, W. Shan, M. Wang, H. Zhou, Z. Feng, K.L. More, G. Wang, D. Su, D.A. Cullen, L. Fei, S. Litster, G. Wu, Single Cobalt Sites Dispersed in Hierarchically Porous Nanofiber Networks for Durable and High-Power PGM-Free Cathodes in Fuel Cells, Adv. Mater. 32 (2020) 2003577, https://doi.org/10.1002/adma.202003577.
17. X.L. Chen, J.W. Huang, Y.C. Huang, J. Du, Y.F. Jiang, Y. Zhao, H.B. Zhu, Efficient Fe-Co-N-C Electrocatalyst Towards Oxygen Reduction Derived from a Cationic Co-II-based Metal-Organic Framework Modified by Anion-Exchange with Potassium Ferricyanide, Chem.-Asian J. 14 (2019) 995-1003, https://doi.org/10.1002/asia.201801776.
18. S. Song, Y. Wang, P. Tian, J. Zang, One-step complexation and self-template strategy to synthesis bimetal Fe/Mn–N doped interconnected hierarchical porous carbon for enhancing catalytic oxygen reduction reaction, Int. J. Hydrogen Energy 47 (2022) 24728-24737, https://doi.org/10.1016/j.ijhydene.2022.05.218.
19. Niu, H.-J.; Wang, A.-J.; Zhang, L.; Feng, J.-J. Bioinspired One-Step Pyrolysis Fabrication of 3D Porous Co, N, P-doped Carbon Nanosheets with Enriched CoNx Active Sites as High-Performance Bifunctional Oxygen Electrocatalyst for Rechargeable Zn–Air Battery. ACS Applied Energy Materials 2020, 3 (3), 2781.
20. Jing Qi, Wei Zhang, Rui Cao, Aligned cobalt-based Co@CoOx nanostructures for efficient electrocatalytic water oxidation, Chem. Commun., 2017, 53, 9277-9280.
21. Peng, X.; Xian, X.; Han, L.; Liu, Y.; Zheng, P.; Fu, Y.; Dong, P.; Zeng, X.; Zhang, Y. Co2P Nanoparticles Encapsulated in N-Doped Carbon Nanotubes as a Bifunctional Oxygen Catalyst for a High-Performance Rechargeable Zn–Air Battery. ACS Applied Nano Materials 2023, 6 (3), 2027.
22. X. Wen, X. Yang, M. Li, L. Bai, J. Guan, Co/CoOx nanoparticles inlaid onto nitrogen-doped carbon-graphene as a trifunctional electrocatalyst, Electrochim. Acta 296 (2019) 830-841
23. Xie, W.; Song, Y.; Li, S.; Li, J.; Yang, Y.; Liu, W.; Shao, M.; Wei, M. Single-Atomic-Co Electrocatalysts with Self-Supported Architecture toward Oxygen-Involved Reaction. Advanced Functional Materials 2019, 29 (50).
24. F. Ming, H. Liang, H. Shi, X. Xu, G. Mei, Z. Wang, MOF-derived Co-doped nickel selenide/C electrocatalysts supported on Ni foam for overall water splitting, J. Mater.

Chem. A, 2016, 4, 15148–15155

25. Ye, D.; Shen, Y.; Mao, H.; Liang, Y.; Gao, Q.; Yang, S.; Zhang, S.; Cai, X.; Fang, Y. Dual-sources directed construction of N-doped carbon nanotube arrays as superior Self-supported bifunctional air electrodes for Rechargeable/Flexible Zinc-air batteries. Chemical Engineering Journal 2023, 464.
26. S. Wang, P. He, L. Jia, M. He, T. Zhang, F. Dong, M. Liu, H. Liu, Y. Zhang, C. Li, J. Gao, L. Bian, Nanocoral-like composite of nickel selenide nanoparticles anchored on two-dimensional multi-layered graphitic carbon nitride: A highly efficient electrocatalyst for oxygen evolution reaction, Appl. Cat. B: Environ. 243 (2019) 463-469
27. Lu, M.; Yang, X.; Li, Y.; Zhu, Z.; Wu, Y.; Xu, H.; Gao, J.; Yao, J. Modulating the Electronic Structure of Porous Nanocubes Derived from Trimetallic Metal–Organic Frameworks to Boost Oxygen Evolution Reaction Performance. Chemistry – An Asian Journal 2019, 14 (19), 3357
28. W. Li, B. Liu, D. Liu, P. Guo, J. Liu, R. Wang, Y. Guo, X. Tu, H. Pan, D. Sun, F. Fang, R. Wu, Alloying Co Species into Ordered and Interconnected Macroporous Carbon Polyhedra for Efficient Oxygen Reduction Reaction in Rechargeable Zinc-Air Batteries, Adv. Mater. 34 (2022) 2109605, https://doi.org/10.1002/adma.202109605.
29. T. Cui, Y.P. Wang, T. Ye, J. Wu, Z. Chen, J. Li, Y. Lei, D. Wang, Y. Li, Engineering Dual Single-Atom Sites on 2D Ultrathin N-doped Carbon Nanosheets Attaining Ultra-Low-Temperature Zinc-Air Battery, Angew Chem. Int. Ed. 61 (2022) 202115219, https://doi.org/10.1002/anie.202115219.
30. L. Huang, L. Zuo, T. Yu, H. Wang, Z. He, H. Zhou, S. Su, T. Bian, Two-Dimensional Co/Co_9S_8 Nanoparticles Decorated N, S Dual-Doped Carbon Composite as an Efficient Electrocatalyst for Zinc-Air Battery, J. Alloy. Compd. 897 (2022) 163108, https://doi.org/10.1016/j.jallcom.2021.163108.
31. C. Yang, S. Shang, Q. Gu, J. Shang, X. Li, Metal-organic framework-derived carbon nanotubes with multi-active Fe-N/Fe sites as a bifunctional electrocatalyst for zinc-air battery, J. Energy Chem. 66 (2022) 306-313, https://doi.org/10.1016/j.jechem.2021.08.019.
32. Q. Yu, H. Li, R. Li, S. Zeng, R. Li, Q. Yao, H. Chen, K. Qu, Y. Zheng, Natural DNA-assisted ultrafine FeP embedded in N, P-codoped carbons for efficient oxygen reduction,

hydrogen evolution and rechargeable zinc-air battery, Carbon 186 (2022) 171-179, https://doi.org/10.1016/j.carbon.2021.09.064.

33. Rong, J.; Gao, E.; Liu, N.; Chen, W.; Rong, X.; Zhang, Y.; Zheng, X.; Ao, H.; Xue, S.; Huang, B.et al. Porphyrinic MOF-derived rich N-doped porous carbon with highly active CoN4C single-atom sites for enhanced oxygen reduction reaction and Zn-air batteries performance. Energy Storage Materials 2023, 56, 165
34. G. Kresse and J. Furthmuller, Physical Review B, 1996, 54, 11169-11186.
35. J. P. Perdew, K. Burke and M. Ernzerhof, Physical Review Letter, 1996, 77, 3865-3868.
36. S. Grimme, Journal of Computational Chemistry, 2006, 27, 1787-1799.
37. J. K. Nørskov, J. Rossmeisl, A. Logadottir, L. Lindqvist, J. R. Kitchin, T. Bligaard and H. Jónsson, *Journal of Physical Chemistry B*, 2004, **108**, 17886–17892.
38. A. Tripathi, C. Hareesh, S. Sinthika, G. Andersson and R. Thapa, *Appl Surf Sci*, DOI: 10.1016/j.apsusc.2020.146964.
39. A. Ruban, B. Hammer, P. Stoltze, H. L. Skriver and J. K. Nørskov, Journal of Molecular Catalysis A: Chemical, 1997, 115, 421-429.
40. J. Chang, Q. Zhang, J. Yu, W. Jing, S. Wang, G. Yin, G. I. N. Waterhouse and S. Lu, Advanced Science, 2023, 10, 2301656.